(i) When the computer is carrying out operations (rather than just trying to remember some state), the decay of quantum coherence is inevitably exponential even in the limit of zero temperature. Nevertheless, (ii) exponential decay is not a reason to give up: It is the rate of that decay that ultimately matters. This rate is given by Eq. 12 in the case studied here, and by $\varepsilon^2 k_B T/\hbar\Delta$ for the temperature-dominated regime. In either case, by increasing isolation (that is, by making ε small) and making the clock rate Δ large, one can take the computation well beyond the time scale (thermal or otherwise) when the loss of coherence becomes exponential with time.

Ultimately, the savior of general-purpose quantum computing lies in the success of quantum error correction. It is generally true that the discrepancy between the correct state of a quantum computer and the actual state will initially increase only quadratically in time (t)

$$|\langle\psi_{\mathrm{actual}}|\psi_{\mathrm{ideal}}\rangle|^2 \simeq 1 - (\delta t)^2 \qquad (13)$$

where δ is the variance of the difference between the ideal and actual energy. Thus, the "watchdog effect" can be used to stabilize the computation (*19*), for when the computer is measured often enough, on a time scale t/ν that is short compared with $1/\delta$, it will stray from the correct evolution only a little, so that the probability of being correct is

$$|\langle\psi_{\mathrm{actual}}|\psi_{\mathrm{ideal}}\rangle|^2 \simeq \left[1 - \left(\frac{\delta t}{\nu}\right)^2\right]^\nu \qquad (14)$$

which can be much closer to unity than Eq. 13. Performing a measurement on a qubit at the instants when it is expected to be in the eigenstate of the measured observable with certainty according to $|\psi_{\mathrm{ideal}}\rangle$ will project the actual state of the computer into a state closer to $|\psi_{\mathrm{ideal}}\rangle$ and may thus offer a way of implementing such a "watchdog stabilization" (*20*). Although this effect is useless once the loss of coherence becomes exponential (as it is for spontaneous emission), such a scheme may be helpful in keeping at bay errors from timing inaccuracies and environmental differences. For example, in the linear ion trap computer (*14*), both the center-of-mass phonon and the auxiliary levels of the ions have predictable occupation numbers at well defined instants during ideal operation. This promise, coupled with the results obtained from our analysis of the impact of decoherence on the quantum factoring algorithm, bring some hope to the eventual reality of quantum computers and motivate further experimental investigations in this field.

REFERENCES AND NOTES

1. R. Graham, D. E. Knuth, O. Patashnik, *Concrete Mathematics* (Addison-Wesley, Reading, MA, 1994).
2. See A. K. Lenstra and H. W. Lenstra, in *Handbook of Theoretical Computer Science*, J. van Leeuwen, Ed. (MIT Press, Cambridge, MA, 1990), vol. A, pp. 673–715. For an opposing argument, see V. R. Pratt. *SIAM J. Comput.* **4**, 214 (1975).
3. A. K. Lenstra and H. W. Lenstra, Eds., *The Development of the Number Field Sieve*, vol. 1554 of *Lecture Notes in Mathematics* (Springer-Verlag, Berlin, 1993).
4. P. W. Shor, in *Proceedings of the 35th Annual Symposium on Foundations of Computer Science*, S. Goldwasser, Ed. (IEEE Computer Society Press, Los Alamitos, CA, 1994), pp. 124–134.
5. R. Landauer, in *Proceedings of the Drexel-4 Symposium on Quantum Nonintegrability: Quantum Classical Correspondence*, D. H. Feng and B.-L. Hu, Eds. (International Press, Boston, 1995).
6. D. Deutsch. *Proc. R. Soc. London Ser. A* **400**, 97 (1985).
7. W. H. Zurek. *Phys. Today* **44**, 36 (October 1991).
8. ———, *Phys. Rev. D* **24**, 1516 (1981); *ibid.* **26**, 1862 (1982).
9. W. H. Zurek, in *Frontiers of Nonequilibrium Statistical Physics*, G. T. Moore and M. O. Scully, Eds. (Plenum, New York, 1986), pp. 151–162.
10. E. A. Lee and D. G. Messerschmitt, *Digital Communication* (Kluwer Academic, Dordrecht, Netherlands, 1988).
11. S. Lloyd, *Science* **261**, 1569 (1993).
12. D. P. DiVincenzo, *Phys. Rev. A* **50**, 1015 (1995).
13. I. L. Chuang and Y. Yamamoto, *ibid.* **52**, 3489 (1995).
14. J. I. Cirac and P. Zoller, *Phys. Rev. Lett.* **74**, 4091 (1995).
15. W. G. Unruh, *Phys. Rev. A* **51**, 992 (1995).
16. A. J. Leggett *et al.*, *Rev. Mod. Phys.* **59**, 1 (1987).
17. J. P. Paz, unpublished results.
18. C. Monroe, D. M. Meekhof, B. E. King, W. M. Itano, D. J. Wineland, "Demonstration of a Universal Quantum Logic Gate," preprint (July 1995).
19. W. H. Zurek, *Phys. Rev. Lett.* **53**, 391 (1984).
20. ———, in preparation.

21. We thank J. Anglin, J. P. Paz, and Y. Yamamoto for useful conversations. I.L.C. acknowledges the support of a fellowship from the Fannie and John Hertz Foundation.

14 February 1995; accepted 10 October 1995

Correlated Variations in the Solar Neutrino Flux and the Solar Wind and the Relation to the Solar Neutrino Problem

R. L. McNutt Jr.

Solar wind parameters from the Massachusetts Institute of Technology (MIT) plasma experiment on the IMP 8 spacecraft overlap ~19 years of published neutrino flux observations from the Homestake experiment. A strong correlation is found between neutrino flux and solar wind properties, in particular, the solar wind mass flux. The correlation is significantly better than any anticorrelation with sunspot number and is comparable to those previously found with photospheric magnetic flux and shifts in *p*-mode frequencies. If current notions of solar structure are correct, these observations require new fundamental physics of neutrinos. For a proper choice of neutrino parameters, the level of variations is consistent with resonant conversion of electron neutrinos to a nondetected flavor eigenstate mediated by the magnetic field in the sun's convective zone. The solar wind mass flux may act as a proxy for this field, producing the solar wind–neutrino flux connection.

The measured average neutrino flux from the sun is low compared with predictions based on solar models. This discrepancy, a factor of more than 3, originally showed up in the data of the ^{37}Cl experiment in the Homestake Gold Mine in South Dakota (*1*) and is known as the solar neutrino problem (*2*). Low neutrino fluxes have been confirmed for neutrino energies other than those measured at Homestake by the Kamiokande-II water Cherenkov experiment (*3*) and the SAGE (*4*) and GALLEX (*5*) gallium experiments.

The Homestake rate appears to exhibit a time-variable component. A possible anticorrelation with solar activity has been studied by a number of investigators. The correlation has remained suspect because of the low counting statistics, questionable correlation, and difficulty of explanation (*6–8*). Confirmation from the other solar neutrino experiments now operating is problematic because of the shorter times the experiments have been running and large statistical uncertainties.

Strong (time-dependent) correlations have been reported between shifts in solar *p*-mode frequencies and the Homestake capture rate (*9*, *10*). Recently an anticorrelation of capture rate with photospheric magnetic flux that is stronger than that with sunspot number has been found (*11*); this anticorrelation increases as flux away from the center of the solar disk is excluded. In this report I show that there is a corresponding large correlation between capture rate and the solar wind flux as measured near Earth by the MIT plasma experiment on the IMP 8 satellite.

The solar wind data used here are from the MIT Faraday cup plasma analyzer (*12*). The only significant data gap is from part of 1982 to 1983, resulting from a problem with

The Johns Hopkins University Applied Physics Laboratory, Laurel, MD 20723–6099, USA.

the instrument-mode setting during that period. The relative calibration of the MIT experiment has remained extremely stable over the years since launch; with the use of continuous data from one instrument on one spacecraft, issues of intercalibration with other measurements were avoided (*13*).

Data acquired in the solar wind were averaged over the periods during which neutrino capture fluxes were monitored for a given run. For composite variables such as the solar wind proton flux, the product of the density and speed was formed from the hourly averaged density and hourly averaged speed, and these were then averaged over the given Homestake run. In all, 62,999 hourly averages were formed into 91 bins, which overlap with neutrino capture runs 31 through 126 (*14*). These averages were used for comparison with the neutrino capture flux data. There are no IMP 8 data during Homestake run 76 because of the instrument problem referred to above (*15*).

The same technique was applied to daily values of the sunspot number for the same time period (*16*). In all, 6796 values of the daily sunspot number were averaged into 92 intervals. These correspond to the same bins used for the solar wind parameters, with the exception that the data for Homestake run 76 was left in the sunspot data set.

Neutrinos were presumed to have sufficiently small masses so that they are relativistic and reach Earth from the sun in ~8 min. Hence, the density and magnetic structure of both the solar wind and the sun through which a given neutrino travels are essentially constant in time during the propagation. The data accumulation intervals for the neutrino runs were also long compared with the solar wind propagation time to Earth (~4 days) and effectively average over the 27-day solar rotation period and subsolar heliolatitude range (±7°15′) as viewed from Earth. Given the typical persistence of solar wind structures over several solar rotations, correlated variations tend to be reinforced in the time periods of the individual Homestake runs; such persistence can also be amplified in the data by averaging.

Use of a boxcar average of the data points (a low-pass filter) improved the apparent significance of the correlations (*6*, *9*, *11*, *17*). Sunspot data and ^{37}Ar capture data are shown in Fig. 1 as a function of time with 3-point sliding boxcar averages. The neutrino capture rate is scaled to the sunspot number from a simple linear regression using the two filtered data sets. The amplitude of the neutrino capture rate variations is significantly reduced in comparison with that of the sunspot number variations. The scaling is from a linear regression with

$$y_\nu = ax_\nu + b \qquad (1)$$

with $a \approx -53.1$ and $b \approx 116$. Here, x_ν are the 3-point sliding averages of the measured neutrino capture rate (equal to the production rate of ^{37}Ar), and y_ν are the scaled values that are plotted in the figure with a and b derived from the linear regression (*18*).

The solar wind (proton) flux and neutrino capture rate are plotted in Fig. 2 with the same format and methodology used for Fig. 1. The scaling of the neutrino flux is given with Eq. 1 and $a \approx 1.15 \times 10^8$ cm^{-2} s^{-1} and $b \approx 3.31 \times 10^8$ cm^{-2} s^{-1}. The tracking of the two variations is much more striking in Fig. 2 than in Fig. 1.

Linear regression analyses were also performed on other solar wind quantities. The largest value of the linear regression coefficient (Pearson's r) occurs for the solar wind particle flux ($r = 0.419$), although it is large for any of the solar wind moments (r = 0.371, 0.375, and 0.354 for the density, momentum flux, and product of density and thermal speed, respectively). Of the quantities examined, only the speed and thermal speed are less well correlated ($r = 0.0843$ and 0.0438, respectively) than the sunspot number ($r = -0.183$; a negative value being an anticorrelation).

This analysis has also been applied to the single data points and 5-point sliding averages. The correlations in the case of the 3-point averages are always better than those from just the individual data points themselves (Table 1). Formal significance levels are extremely small for the sliding averages, but the low-pass filtering (by means of the sliding average) introduces additional correlations between points, reducing the true number of degrees of freedom. For the solar wind mass flux, the 3-point sliding average r and 30 points yield a significance P of 0.021; the 5-point regression and 18 effective points yield a significance of 0.088.

Reported correlations with emergent magnetic flux (*11*) used 5-point running averages over the period 1970.3 through 1991.6. Excluding regions with heliographic latitudes in excess of 5°, the Spearman correlation coefficient was −43%, not quite as large (in magnitude) as values obtained with the solar wind mass flux correlation for both 3- and 5-point sliding averages (Table 2). Comparable correlations and significance levels with respect to other solar phenomena have also relied on similar methodology (*10*).

As a check on the results, nonparametric tests were applied to the solar wind flux and sunspot number (Table 2) for each averaging interval (again 1-, 3-, and 5-point sliding averages in the time series). These nonparametric analyses confirm the linear re-

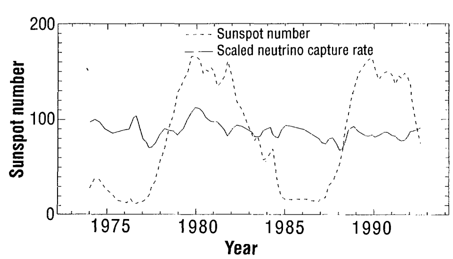

Fig. 1. Sunspot number and neutrino capture rate (^{37}Ar capture data) as a function of calendar year. The period covered starts with the beginning of the IMP 8 mission and goes through the end of the published neutrino capture data. The neutrino capture rate has been scaled to the sunspot number average in the neutrino-run bins based on a simple linear regression, which is based on 3-point sliding averages of the binned data (Eq. 1). Note that the neutrino capture rate is inverted because the correlation coefficient is negative. The end points not averaged over have been suppressed.

Table 1. Linear regression results. Averages are sliding boxcar averages of both binned data sets: 92 bins are used for the sunspot data (based on daily sunspot number) and 91 bins are used for solar wind data (based on hourly averages of proton density and proton speed). Probabilities P are two-sided significance levels for the acceptance of the null hypothesis (that is, that the data sets are uncorrelated). The z is from Fisher's z transformation and can be used to compare the significance levels (*18*).

Average	Sunspots			Particle flux		
	r	z	P	r	z	P
1-point	−0.143	−0.144	0.174	0.202	0.205	0.0543
3-point	−0.183	−0.186	0.0800	0.419	0.446	3.60×10^{-5}
5-point	−0.213	−0.217	0.0411	0.414	0.440	4.52×10^{-5}

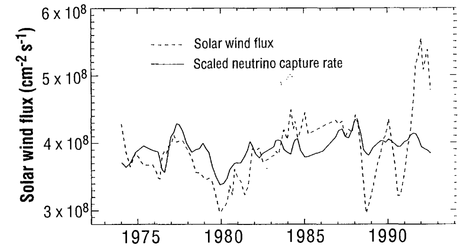

Fig. 2. Solar wind proton flux and neutrino capture rate as a function of calendar year. The neutrino capture rate is scaled to the solar wind flux with linear regression parameters from 3-point sliding averages of the binned data.

sults: lack of correlation (the null hypothesis) between the solar wind flux and the neutrino capture rate is very unlikely (less than 3%) with the individual 91 data points. This probability compares with less than 17% for a sunspot correlation.

Since the early 1960s, the density, velocity, and temperature of the solar wind near Earth orbit have been monitored with varying degrees of regularity. Long-term variations in these quantities are difficult to monitor because of (i) the small amplitudes of long-term variations, (ii) large short-term variations, (iii) incomplete data coverage, and (iv) inherent difficulties in intercalibrating different instruments on different satellites (*19*). Over the long term, the solar wind mass flux does not vary greatly, consistent with the results reported here. Mass flux is known to vary with solar wind speed, and the distribution of wind speed in heliographic latitude and longitude varies with the phase of the solar cycle (*20*). Hence, some variation of the mass flux as seen at Earth can be ascribed to the excursion of Earth (and therefore IMP 8) in heliographic latitude.

The near constancy of the solar wind mass flux observed near the ecliptic plane is linked to coronal dynamics that couple to solar magnetic field structure at lower levels. Variations are the result of varying expansion factors in magnetically open regions (*21*): the larger the magnetically open regions, the less the areal expansion and the larger the mass flux. Although the mass flux and coronal-hole characteristics and filling factors vary with solar activity, a clear-cut oscillatory behavior in the these quantities is not present. Hence, a correlation between solar wind properties and the neutrino capture flux, both of which exhibit aperiodic behavior, appears all the more remarkable.

A consistent picture is emerging in which increased neutrino flux corresponds to (i) decreased line-of-sight magnetic flux (*11*), (ii) decreased *p*-mode frequencies (*9*, *10*), (iii) decreased sunspot number (*6*, *7*), (iv) increased solar radius (*10*), and (v) increased proton and mass flux in the solar wind (this work). Internal consistencies exist in this list as well: (i) and (ii) (*22*), (ii) and (iv) (*10*), (ii) and (iii) (*23*), and (i) and (iii) (*11*) are each consistent.

The model of (*24*) suggests that the average radial component of the photospheric magnetic field B_r decreases with *p*-mode frequencies as observed (*11*). In spherically symmetric solar wind models, the ratio of mass flux to radial magnetic-field component is a field-line constant, so larger B_r implies larger flux. However, this is a local argument and does not take closed fields into account. Observations show that the mass flux at the coronal base tends to increase linearly with the (radial) magnetic field there. Similarly, the logarithm of the mass flux there tends to increase roughly quadratically with the flux-tube expansion factor (*25*). These combined effects result in a larger photospheric magnetic field correlated with a smaller magnetic flux at Earth, that is, less (net) radial flux (fewer closed regions) should correspond to lower areal expansion factors (*21*) and larger solar wind flux, as observed. All of these observed variations tend to decrease if larger averaging intervals are used.

The correlation study with photospheric magnetic flux supports the hypothesis that the neutrinos interact with magnetic fields along their flight paths (*11*). This hypothesis is also supported by observations of the solar wind mass flux at Venus. Measurements are available from the plasma analyzer on the Pioneer Venus Orbiter (PVO) spacecraft from orbit insertion in 1978 through orbit decay in 1992 (Fig. 3).

The PVO data are offset from, but track, the IMP 8 data from the beginning of 1979 through 1985. From 1985 through the beginning of 1988, the PVO mass flux differs dramatically from both the IMP 8 flux and scaled neutrino count rate. During this period, PVO (and Venus) were immersed in a low-speed, high-density solar wind usually associated with the equatorial streamer belt, whereas IMP 8 (and Earth) spent most of this period at higher heliolatitudes and observed different wind properties (*26*) (the excursion of Venus from the solar equator is less than that of the Earth, only ~4°). Both

Table 2. Nonparametric statistical tests for solar wind flux and sunspots. The same data are used as in Table 1. Here, r_{Spearman} is Spearman's rank correlation coefficient; σ_D, the variance of sum squared difference of ranks; τ, Kendall's τ; σ_τ, the variance in the τ statistic; and P_{rs}, P_D, and P_τ, the corresponding signifiance levels for these statistics (*18*).

Average	r_{Spearman}	P_{rs}	σ_D	P_D	τ	σ_τ	P_τ
			Solar wind flux				
1-point	0.233	0.0263	−2.21	0.0269	0.155	2.17	0.0297
3-point	0.440	1.29×10^{-5}	−4.17	3.00×10^{-5}	0.308	4.33	1.50×10^{-5}
5-point	0.450	7.4×10^{-6}	−4.27	1.92×10^{-5}	0.323	4.53	5.8×10^{-6}
			Sunspots				
1-point	−0.144	0.170	1.37	0.170	−0.112	−1.58	0.113
3-point	−0.0801	0.448	0.763	0.446	−0.0588	−0.830	0.406
5-point	−0.126	0.232	1.20	0.223	−0.0855	−1.21	0.227

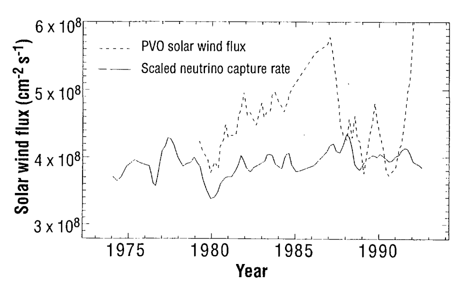

Fig. 3. Solar wind proton flux at Venus as monitored by the plasma analyzer on board PVO. The scales and neutrino capture rate are duplicated from Fig. 2. The PVO data overlap Homestake runs 57 through 125; 66 runs actually overlap. Solar wind parameters were obtained from Ames Research Center (by means of the World Wide Web) and processed in the same manner as the IMP 8 data; the mass flux is decreased by a factor of $(0.72)^2$ to normalize the data to 1 AU. The PVO fluxes are generally higher than those from IMP 8 because of unmodeled instrument offsets.

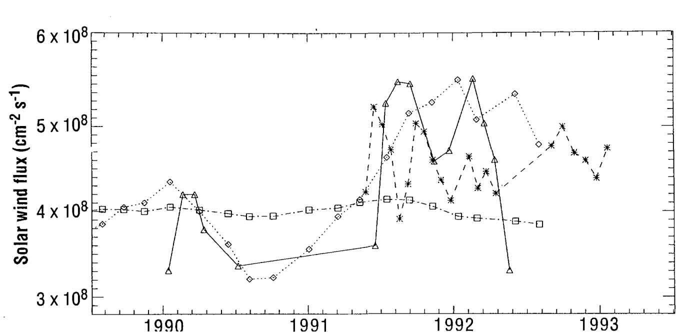

Fig. 4. Comparison of relative count rates from the gallium experiments [GALLEX (*) and SAGE (△)] with solar wind flux variations (◇). The same conversion to mass flux as found from the Homestake data (□) is applied but reduced by an arbitrary factor of 80; error bars on each measurement are comparable to the measurements themselves. All data are shown as 3-point sliding averages (see Fig. 2). The SAGE results include 15 runs from January 1990 through May 1992 (*4*). There is no reported statistical evidence for variations in the background; the average rate is $73\,^{+18}_{-16}$ (statistical) $^{+5}_{-7}$ (systematic) solar neutrino units (1 SNU = 10^{-36} captures per target atom per second). GALLEX results include 21 runs made from 14 May 1991 through 3 February 1993 (*5*). Combined analysis for all runs is 87 ± 14 (statistical) ± 7 (systematic) SNU. More recent results are 79 ± 12 SNU; the standard model prediction for gallium experiments is 132 ± 7 SNU (*2*).

low-speed flows and high-speed streams are nonradial near the sun (*20*) and are not necessarily representative of the region traversed along a radial path by the neutrinos. Such flow and solar activity not linked to the neutrino modulation mechanism could explain the relatively worse correlation between solar wind and neutrino fluxes in Figs. 2 and 3 from ~1988 through the end of the data in 1992 (part of the increase at the end of 1991 is an artifact associated with the end of the PVO mission before entry into the atmosphere of Venus).

The SAGE data runs (Fig. 4) have no counting events during times of low solar wind flux. High rates are found during the summer of 1991 (and in Homestake run 117), coincident with major solar activity that produced radio emissions from the outer heliosphere, although this is also the period that the correlation of the Homestake data with the solar wind mass flux is not as good as for previous periods. However, the peak rates in the radiochemical experiments occur in nominally nonoverlapping runs. Furthermore, similar solar activity levels in mid-1982 through early 1983 produced no correspondingly anomalous rates in Homestake runs at corresponding times (runs 75 and 76) (*27*). The relatively few data points and large counting and systematic errors make identification of temporal variations problematic. No consistent pattern of time variation is suggested by either the peak values or the current series of gallium detector data. There may be a suggestion of a correlation between the IMP 8 and SAGE data, with some lag in the solar wind data. There has been no significant time variation reported in the Kamiokande-II experiment (*3*).

Proposed solutions to the solar neutrino problem can be classified as astrophysical or nonastrophysical. Astrophysical solutions posit that the production rate of the neutrinos is not calculated correctly because of some fundamental flaw in our understanding of how the sun produces energy. Suppressed or fluctuating neutrino fluxes result from conditions in the solar core (*6*). However, these solutions are not consistent with detailed results from helioseismology (*28*). Nonastrophysical solutions suppose that the production rate of the neutrinos is calculated correctly (*8*), that there is no link between the solar core and (short-term) photospheric variations, and that the suppressed fluxes monitored at Earth are caused by neutrino physics outside of the standard model of electroweak interactions (*8, 28, 29*).

The variations in *p*-mode splittings, emergent magnetic flux, and solar wind flux with the neutrino capture flux suggest a connection between solar activity and extended neutrino physics in the convective zone of the sun (*30*). The observed time variations do not support other nonastrophysical solutions (*8*).

Although a magnetic moment is acquired by massive Dirac neutrinos, it is too small to couple effectively to the solar magnetic field. A further extension of electroweak theory can provide sufficiently large magnetic moments $\mu_\nu \sim 10^{-10}\mu_{\rm Bohr}$ (*30*) (where $\mu_{\rm Bohr}$ is the Bohr magneton), although such large values may violate limits derived from neutrino observations of supernova SN 1987A (*31*). Energy and time dependencies are coupled to this solution if neutrinos are massive and if the spin-flip is moderated by a resonance similar to that in the MSW (Mikheyev-Smirnov-Wolfenstein) effect (*32*).

If the mass difference parameter $\Delta_0 \equiv m_2^{\,2} - m_1^{\,2} > 0$ is sufficiently small for convection zone resonance (*32, 33*), then all of the fusion neutrinos are born well above their resonant density. The survival probability of electron neutrinos (ν_e) can be estimated as (*32*)

$$P(\nu_e \rightarrow \nu_e) \approx \frac{1}{2} - \frac{\frac{1}{2} - e^{-\pi^2 r_0 L_{\rm osc}/L_B^2 \cos 2\theta}}{\sqrt{1 + L_{\rm osc}^2/L_{B0}^2 \cos^2 2\theta}} \qquad (2)$$

where the argument of the exponential is evaluated at the resonant density (*34*). For a spatially varying magnetic field, the effective vacuum value B_0 is less than the resonant value $B_{\rm res}$ and should be about the same for all neutrinos, whereas $B_{\rm res}$ varies with energy because the magnetic field, a function of location, varies with the resonant density.

As an example (Fig. 5), for $\Delta_0\cos(2\theta) \sim 10^{-8}$ eV^2 and $\mu_\nu \sim 1.5 \times 10^{-10}\ \mu_{\rm Bohr}$, plausible levels and variations in the survival probability can be reproduced. All neutrinos pass through an MSW resonance as well (*32*), but the resonance is nonadiabatic and has no effect. Intermediate energy neutrinos are both suppressed and modulated the most (*2*); low-energy neutrinos (*4, 5*) are not suppressed as much because most of them pass through corresponding resonances in the radiative zone (*32*), where the magnetic field strength is small. Small penetrations of large field strengths to lower levels could produce large excursions in neutrino flux. Less time variation occurs in the higher energy neutrinos (*3*). Measured suppression levels can be explained by detection of the converted neutrinos but with less efficiency (*33*). The solar wind mass flux is a proxy for the magnetic field strength in the convection zone (Eq. 2) and provides the physical link between the solar wind and neutrino fluxes.

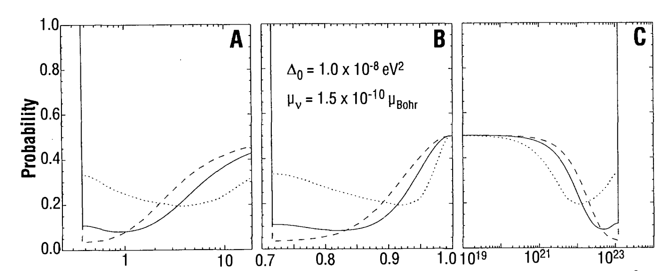

Fig. 5. (**A**) Model calculation of the probability of electron neutrino survival as a function of energy from the ^{71}Ga threshold (0.2332 MeV) to the cutoff energy for *hep* neutrinos (18.77 MeV) (*8*). The electron density is constructed from models in (*8*) and (*36*). The (toroidal) magnetic field is taken to vary as $B \sim n_e^{1/6}$ (n_e, number density of electrons) throughout the convective zone and is normalized to 2.5 kG at 0.91 times the radius of the sun (*24*); B_0 is set to 1.0 kG and the magnetic field is set to zero everywhere inside the convective zone [assuming the solar dynamo is confined there (*30*)]. The solid line shows the survival probability for "average" field conditions. The dashed line corresponds to a field strength that is 30% higher than average, and the dotted line, to a strength 30% lower than average for the neutrino parameters shown. (**B**) and (**C**) show the same probability as a function of the radial location of the spin-flip resonance and the corresponding resonant density, respectively.

REFERENCES AND NOTES

1. R. Davis, *Prog. Part. Nucl. Phys.* **32**, 13 (1994).
2. R. S. Raghavan, *Science* **267**, 45 (1995); J. N. Bahcall *et al.*, *Nature* **375**, 29 (1995).
3. K. S. Hirata *et al.*, *Phys. Rev. Lett.* **65**, 1297 (1990).
4. J. N. Abdurashitov *et al.*, *Phys. Lett. B* **328**, 234 (1994).
5. P. Anselmann *et al.* (GALLEX Collaboration), *ibid.* **314**, 445 (1993).
6. W. R. Sheldon, *Nature* **221**, 650 (1969); K. Sakurai, *ibid.* **278**, 146 (1979); *Sol. Phys.* **74**, 35 (1981); L. J. Lanzerotti and R. S. Raghavan, *Nature* **293**, 122 (1981); G. A. Bazilevskaya, Yu. I. Stozhkov, T. N. Charakhch'yan, *JETP Lett.* **35**, 341 (1982); V. N. Gavrin, Yu. S. Kopysov, N. T. Makeev, *ibid.*, p. 608; P. Raychaudhuri, *Sol. Phys.* **106**, 421 (1986); R. M. Wilson, *ibid.* **112**, 1 (1987); J. W. Bieber *et al.*, *Nature* **348**, 407 (1990).
7. J. N. Bahcall and W. H. Press, *Astrophys. J.* **370**, 730 (1991).
8. J. N. Bahcall, *Neutrino Astrophysics* (Cambridge Univ. Press, New York, 1989).
9. L. M. Krauss, *Nature* **348**, 403 (1990).
10. Ph. Delache *et al.*, *Astrophys. J.* **407**, 801 (1993).
11. D. S. Oakley, H. B. Snodgrass, R. K. Ulrich, T. L. Van De Kop, *ibid.* **437**, L63 (1994).
12. The IMP 8 (Interplanetary Monitoring Platform, also designated Explorer 50) was launched on 26 October 1973, began to gather data shortly thereafter, and continues to operate. The spacecraft orbits Earth at roughly 30 Earth radii in ~2 weeks. About two-thirds of this time is spent in the solar wind and the other one-third in the Earth's magnetosphere.
13. K. I. Paularena and A. J. Lazarus, *J. Geophys. Res.* **99**, 14777 (1994).
14. Data from runs 18 through 22, 24, 27 through 33, 35 through 92, and 94 through 99 are from tables 10.3 and 10.5 of (*8*). The data from nominal run 90 were used (showing an ^{37}Ar production rate of 0.0), and run 93 was not included. The ^{37}Ar production rates

for runs 100 through 103 were scaled from figure 1 of (7). The ^{37}Ar rates for runs 104 through 114 were scaled from figure 1 of (35). Data for runs 115, 116, 118 through 122, and 124 through 126 were taken from figure 6 of (1). The average solar neutrino capture rate over all 91 runs used differs slightly from the best average for all the available Homestake data (1); including Homestake data from before the IMP 8 launch gives a different average. In the joint Homestake–IMP 8 data, the average neutrino capture rate is 0.527 captures per day with a standard deviation of 0.315 captures per day.

15. Corresponding values for the solar wind flux are 3.91 $\times 10^8$ and 0.67 $\times 10^8$ cm^{-2} s^{-1} for the 91 points used in the two sets. There is no significant skew to either data set.
16. Values from the beginning of 1973 through the end of March 1991 were obtained originally from the Solar Environment Laboratory (National Atmospheric and Oceanic Administration) in Boulder, CO, and were updated through the end of September 1994 with daily sunspot numbers obtained from the National Geophysical Data Center by means of the World Wide Web.
17. B. T. Cleveland *et al.*, in *Proceedings of the 25th International Conference on High Energy Physics* (World Scientific, Teaneck, NJ, 1991), pp. 667–675.
18. W. H. Press, B. P. Flannery, S. A. Teukolsky, W. T. Vetterling, *Numerical Recipes* (Cambridge Univ. Press, New York, 1986).
19. M. Neugebauer, *Space Sci. Rev.* **17**, 221 (1975); H. S. Bridge, *Physics of Solar Planetary Environments*, D. J. Williams, Ed. (American Geophysical Union, Washington, DC, 1976), vol. 1, p. 47; W. C. Feldman, J. R. Asbridge, S. J. Bame, J. T. Gosling, *The Solar Output and Its Variations*, O. R. White, Ed. (Associated Univ. Press, Boulder, CO, 1977), p. 351; P. R. Gazis, *Geophys. Res. Lett.* **21**, 1743 (1994).
20. R. Woo and R. M. Goldstein, *Geophys. Res. Lett.* **21**, 85 (1994); R. Woo and P. R. Gazis, *ibid.*, p. 1101.
21. G. L. Withbroe, *Astrophys. J.* **337**, L49 (1989).
22. M. F. Woodard, J. R. Kuhn, N. Murray, K. G. Libbrecht, *ibid.* **373**, L81 (1991).
23. Y. Elsworth, R. Howe, G. R. Isaak, C. P. McLeod, R. New, *Nature* **345**, 322 (1990).
24. P. Goldreich, N. Murray, G. Willette, *Astrophys. J.* **370**, 752 (1991).
25. Y.-M. Wang, *ibid.* **449**, L157 (1995).
26. P. R. Gazis, *J. Geophys. Res.* **100**, 3383 (1995).
27. R. L. McNutt Jr., *Geophys. Res. Lett.* **15**, 1307 (1988); D. A. Gurnett, W. S. Kurth, S. C. Allendorf, R. L. Poynter, *Science* **262**, 199 (1993); R. L. McNutt Jr. *et al.*, *Adv. Space Res.* **16**(9), 303 (1995).
28. Y. Elsworth, R. Howe, G. R. Isaak, C. P. McLeod, R. New, *Nature* **347**, 536 (1990); W. A. Dziembowski, P. R. Goode, A. A. Pamyatnykh, R. Sienkiewicz, *Astrophys. J.* **445**, 509 (1995).
29. L. Wolfenstein, *Phys. Rev. D* **17**, 2369 (1978); S. P. Mikheev and A. Yu. Smirnov, *Sov. Phys. Usp.* **30**, 759 (1987); J. N. Bahcall and W. C. Haxton, *Phys. Rev. D* **40**, 931 (1989); J. N. Bahcall and H. A. Bethe, *ibid.* **47**, 298 (1993); C. W. Kim and A. Pevsner, *Neutrinos in Physics and Astrophysics* (Harwood Academic, Langhorne, PA, 1993).
30. A. Cisneros, *Astrophys. Space Sci.* **10**, 87 (1971); M. B. Voloshin, M. I. Vysotskii, L. B. Okun, *Sov. Phys. JETP* **64**, 446 (1986).
31. R. Barbieri and R. N. Mohapatra, *Phys. Rev. Lett.* **61**, 27 (1988); J. M. Lattimer and J. Cooperstein, *ibid.*, p. 23; R. Barbieri, R. N. Mohapatra, T. Yanagida, *Phys. Lett. B* **213**, 69 (1988).
32. C.-S. Lim and W. J. Marciano, *Phys. Rev. D* **37**, 1368 (1988); E. Kh. Akhmedov, *Phys. Lett. B* **213**, 64 (1988).
33. H. Minakata and H. Nunokawa, *Phys. Rev. Lett.* **63**, 121 (1989); M. Fukugita and T. Yanagida, *ibid.* **65**, 1975 (1990); Y. Ono and D. Suematsu, *Phys. Lett. B* **271**, 165 (1991).
34. Parameters: r_0 is the scale length for density variations; L_{osc}, the vacuum oscillation length; L_B, the oscillation length in a magnetic field; and θ, the vacuum mixing angle.
35. R. Davis Jr., *Proceedings of the 23rd International Cosmic Ray Conference* (1993), vol. 3, p. 869.
36. H. C. Spruit, *Sol. Phys.* **34**, 277 (1974).
37. This work has taken place over a number of years. Analysis of the relevant solar wind data has been supported under a variety of contracts and grants from the National Aeronautics and Space Administration, including NAGW-1550 through task SC-A-276029 from MIT to Visidyne, task SC-A-383689 from MIT to the Johns Hopkins University Applied Physics Laboratory, under Task I of Navy Contract N00039-91-C-001. I especially acknowledge both the original principal investigator (PI) on the IMP 8 solar wind experiment, H. S. Bridge, the current PI, A. J. Lazarus, and K. I. Paularena (all of MIT) for access to, provision of, and discussions about the IMP 8 plasma data. J. McKinnon provided an initial set of daily sunspot numbers in 1991. I also thank J. Wakefield for calling my attention to the recent review of R. S. Raghavan. D. Rust and C. Keller referred me to the convection zone model of Spruit. I also thank E. Roelof for discussions and comments on the text, D. Rust and M. Dubin for their comments and suggestions, and P. R. Gazis for discussions and access to the PVO plasma data through the Ames Research Center Pioneer Project. Professor Bridge passed away 30 August 1995; this work would not have been possible without him.

16 June 1995; accepted 10 October 1995

AFM Fabrication of Sub-10-Nanometer Metal-Oxide Devices with in Situ Control of Electrical Properties

E. S. Snow and P. M. Campbell

Metal wires and metal-oxide-metal junctions were fabricated by anodic oxidation with the conducting tip of an atomic force microscope (AFM). The width of the wires and resistance of the junctions were controlled by real-time, in situ measurement of the device resistance during fabrication. Because the properties of nanometer-scale devices are very sensitive to size variations, such measurements provide a more accurate method of controlling device properties than by controlling geometry alone. In this way, structures with critical dimensions of less than 10 nanometers were fabricated with precisely tailored electrical properties.

The electrical characteristics of device structures with feature sizes of 10 nm or less are extremely sensitive to variations in size. Because of this sensitivity to local geometry, reproducible device characteristics require near-atomic control of the fabrication. Although a few lithographic techniques can produce features in the 10-nm size regime (*1*), it is unlikely that one can achieve reproducible device properties in such small structures through control of device geometry alone. However, the use of a high-resolution processing technique in conjunction with real-time in situ measurement of device properties during critical fabrication steps as feedback for process control should allow the fabrication of devices with features smaller than 10 nm with precisely tailored electrical properties.

To implement such an approach, we need a fabrication process that does not interfere with the measurement of device properties during fabrication. One such process is atomic force microscope (AFM)–based anodic oxidation, a relatively new technique that has proven useful for lithography and device fabrication in the sub-100-nm size regime (*2, 3*). An electrically biased AFM tip in contact with a surface is used under ambient humidity to produce a local surface oxide. Because the oxidation process produces no measurable current flow between the tip and sample, and because the technique can produce small feature sizes with no proximity effects (*2*), this process is well suited for the tailoring of small structures controlled by in situ electrical measurements.

Naval Research Laboratory, Washington, DC 20375, USA.

In this report, we describe the use of in situ electrical measurements to control the fabrication of metal-oxide device structures with feature sizes ~10 nm. We used AFM anodic oxidation of thin Ti films to fabricate fine metal wires and Ti-TiO_x-Ti lateral junctions. Both the wire width and the junction resistance are controlled by in situ real-time measurement of the device resistance. In this way, metal wires with widths of 5 to 10 nm were achieved with predetermined resistance values. Such structures demonstrate the potential of in situ electrical measurements to produce devices of size $\leq$10 nm with precisely controlled electrical properties.

The scanning tunneling microscope (STM) under appropriate bias conditions can be used to selectively oxidize nanometer-sized regions of a H-passivated Si surface (*4*). A similar technique can be used to oxidize the surface of deposited Ti films (*5*); this oxidation process can completely penetrate suitably thin Ti films to produce lateral metal-oxide-metal device structures with variable junction resistance (*6*). Recently, such junctions were used to fabricate a single-electron tunneling device that was operational at room temperature (*7*). Because these and similar structures require feature sizes of order 10 nm, it is necessary to develop fabrication schemes such as de-